第 48 卷第 1 期　　硅　酸　盐　学　报　　Vol. 48，No. 1
2020 年 1 月　　JOURNAL OF THE CHINESE CERAMIC SOCIETY　　January，2020
http://www.gxyb.cbpt.cnki.net　　**DOI**：10.14062/j.issn.0454-5648.20190166

橙红色荧光粉 $K_2Bi_{1-x}Zr(PO_4)_3$:xSm^{3+}的电子结构与荧光性能

刘小星[1]，赵　丹[2]

(1. 河南理工大学材料科学与工程学院，河南 焦作 454000；
2. 河南理工大学化学与化工学院，河南 焦作 454000)

摘　要：采用常规固相反应合成了无水钾镁矾基荧光粉材料钐(+3)激活磷酸锆铋钾，并用 X 射线衍射、紫外–可见漫反射光谱、密度泛函理论计算(DFT)和光致发光谱等方法进行了研究。DFT 计算表明，磷酸锆铋钾是一种具有间接带隙的绝缘体，带宽为 4.26 eV，适合作为荧光主体材料。该荧光粉可被 340～425 nm 范围内近紫外光有效地激发，发射出一系列钐(+3)的特征发射峰。主要包括 562、600、647 nm 附近 3 个发射带，分别对应于钐(+3)离子 $^4G_{5/2}\rightarrow{}^6H_J$ (J = 5/2, 7/2, 9/2) 的能级跃迁。通过改变 x 值制备了不同钐(+3)浓度的样品，并比较了其发射强度，得出钐(+3)的最佳掺杂浓度为 10%(摩尔分数)。因此，钐(+3)激活磷酸锆铋钾材料可作为橙红色荧光粉在照明和显示领域具有一定的应用价值。

关键词：磷酸盐；荧光粉；密度泛函理论计算；光致发光；钐(+3)激活剂
中图分类号：O483.31　　**文献标志码**：A　　**文章编号**：0454–5648(2020)01–0028–07
网络出版时间：2019–08–29



Electronic Structure and Fluorescence Performance of Orange-Reddish Phosphor $K_2Bi_{1-x}Zr(PO_4)_3$:xSm^{3+}

LIU Xiaoxing[1], *ZHAO Dan*[2]
(1. School of Materials Science and Engineering, Henan Polytechnic University, Jiaozuo 454000, Henan, China;
2. School of Chemistry and Chemical Engineering, Henan Polytechnic University, Jiaozuo 454000, Henan, China)

Abstract: Langbeinite-type $K_2Bi_{1-x}Zr(PO_4)_3$:xSm^{3+} phosphors were synthesized by a conventional solid-state reaction. The samples were characterized by X-ray diffraction, ultraviolet visible diffuse reflectance spectroscopy, calculation based on the density functional theory (DFT), and photoluminescence spectroscopy. The DFT analysis reveals that $K_2BiZr(PO_4)_3$ is an insulator with an indirect band gap of 4.26 eV, which can be used as a fluorescent host. The prepared phosphors can be efficiently excited by near-ultraviolet light in the region from 340 to 425 nm and show three dominant emission bands peaking at 562, 600 and 647 nm due to the $^4G_{5/2}\rightarrow{}^6H_J$ (J = 5/2, 7/2, and 9/2) transition of the Sm^{3+} activator, respectively. The optimum doping concentration of Sm^{3+} is 10% (in mole). It is expected that Sm^{3+}-doped $K_2BiZr(PO_4)_3$ can be used as an orange-reddish phosphor for illumination or displays.

Keywords: phosphate; phosphor; density functional theory calculation; photoluminescence; samarium (3+) activator

1　Introduction

Developing rare-earth activated inorganic luminescent materials has always been a hot topic because of their indispensable applications in biological labeling, plasma display panels (PDPs), field emission displays (FED), and white light-emitting diodes (LEDs) [1–5]. In particular, white LEDs are rapidly replacing

收稿日期：2019–03–19。　修订日期：2019–04–02。
基金项目：国家自然科学基金(21201056)。
第一作者：刘小星(1980—)，男，硕士，讲师。
通信作者：赵　丹(1982—)，男，博士，副教授。

Received date: 2019–03–19.　**Revised date:** 2019–04–02.
First author: LIU Xiaoxing (1980–), male, Master, Lecturer.
E-mail: liuxiaoxing80@163.com
Correspondent author: ZHAO Dan (1982–), male, Ph.D., Associate Professor.
E-mail: iamzd1996@163.com

traditional incandescent and fluorescent lamps due to their environmental friendliness, eco-friendly features, long lifetimes, dependable stability and high efficiency. An efficient method to construct white LEDs is to combine an ultraviolet (UV)-emitting chip with three color phosphors. Therefore, investigations or new investigations on single host phosphors excited by UV or near-UV light have attracted much attention because of their high efficiency, good color rendering index, and stable color tone [6–7]. As one kind of host material, phosphate compounds have received much attention recently in many fields due to their many positive factors, including simple preparation method, structural diversity, high chemical stability and a suitable band gap.

The basic building block of phosphate compounds is the PO_4 group, which is flexible and can inhibit various coordination environments by altering the P–O bond distances in the range of 0.144–0.164 nm. To date, more than four thousand phosphate compounds have been reported, in which the PO_4 group can be further interlinked by corner-sharing the vertex O atoms into various polyphosphate groups, namely, P_2O_7, P_3O_9, P_3O_{10}, P_4O_{13}, P_6O_{18}, 1D chain $(PO_3)_\infty$, ring P_nO_{3n} and so on[8–11]. Introducing different elements into a phosphate structure will generate various kinds of functional materials. For example, the association of MO_6 (transition or rare-earth metal octahedra) with a PO_4 tetrahedra will generate a three-dimensional open framework structure with the cubic space group $P2_13$, namely, a langbeinite-type structure, such as $K_2M_{0.5}Ti_{1.5}(PO_4)_3$ (M=Mn, Co) [12], $K_2FeZrP_3O_{12}$ [13], and $K_2LnZr(PO_4)_3$ (Ln = Ce-Yb, Y, Bi) [14]. A member of the langbeinite-type family, $K_2BiZr(PO_4)_3$ has been reported by Chornii et al[15]. However, there are no reports regarding the detailed photoluminescence properties of activated by rare-earth ions. In this work, we report the synthesis, crystal structure, electronic structure and Sm^{3+}-activated fluorescence performance of a $K_2BiZr(PO_4)_3$ host material.

2 Experimental

2.1 Materials and instrumentation

All reacting ingredients, K_2CO_3 (≥99.00 %, in mass, the same below), Bi_2O_3 (≥99.00 %), ZrO_2 (≥99.00 %), $NH_4H_2PO_4$ (≥99.00 %) and Sm_2O_3 (≥99.99 %) were purchased from Jinan Henghua Technology Co., Ltd., China. The sizes and morphologies of the phosphors were inspected using a scanning electron microscope (Carl Zeiss AG, Merlin Compact). X-ray powder diffraction (XRD) analysis was performed using a Rigaku SmartLab 9 kW diffractometer with graphite-monochromatic Cu K_α characteristic radiation operating at 200 mA and 40 kV; the scanning speed, step length and diffraction range were 10 (°) /min^{-1}, 0.02° and 5°–75°, respectively. Infrared (IR) data were recorded on a Bruker Tensor 27 spectrophotometer (Bruker Optics, Munich, Bavaria, Germany) with KBr pellets in the region of 350–1 700 cm^{-1}. The ultraviolet–visible (UV–Vis) spectrum was measured using a Jascov-550 double beam spectrophotometer in the range of 200–800 nm. Photoluminescence excitation (PLE) and emission (PL) spectra were carried out by a FLuorolog-3 combined time resolved and steady state fluorescence spectrometer (Horiba Company, USA). The measurements were performed using a standard 450 W continuous-wave xenon lamp as the excitation source. A step width of 1 nm and an integration time of 0.2 s were used for the PL excitation and emission spectra measurements.

2.2 Synthetic procedures

The $K_2Bi_{1-x}Zr(PO_4)_3$:xSm^{3+} (x=0, 0.02, 0.04, 0.06, 0.08, 0.10, 0.12, 0.14) samples were synthesized by a traditional high-temperature solid-state reaction method. Stoichiometric amounts of K_2CO_3, Bi_2O_3, ZrO_2, $NH_4H_2PO_4$ and Sm_2O_3 were blended and ground thoroughly in an agate mortar, and the homogeneous mixtures were preheated in alumina crucibles for 4 h at 500 ℃ to decompose K_2CO_3 and $NH_4H_2PO_4$. When cooling to room temperature, the presintered mixtures were ground and heated at 820 ℃ for 40 h, cooled to room temperature naturally, and then crushed to a fine powder for further measurements.

2.3 Computational descriptions

The single crystal data of $K_2BiZr(PO_4)_3$ reported by Chornii et al. [15]. was used to conduct a total energy calculation by CASTEP code [16] without a geometry optimization. The calculation employs pseudopotentials to describe electron-ion interactions and uses a plane-wave basis set for electronic wave functions. The generalized gradient approximation (GGA) with the Perdew-Burke-Ernzerhof (PBE) functional was used for the exchange-correlation potential [17]. A plane-wave basis set energy cutoff was 750 eV within the norm-conserving pseudopotential [18]. The total energy and the force convergence thresholds were 1.0×10^{-6} eV/atom and 0.5 eV/nm. The k-point set meshes to define the number of integration points that will be used to integrate the wave function in reciprocal space were 2×2×2 for calculating the bond structure and density of states [19]. The remainder of the parameters used in the calculations were set by the default values of the CASTEP code. Pseudo atomic calculations were performed for K $3s^23p^64s^1$, Bi $5d^{10}6s^26p^3$, Zr $4s^24p^64d^25s^2$, P $3s^23p^3$ and O $2s^22p^4$.

3 Results and discussion

3.1 Crystal structure

The representative XRD patterns of polycrystalline $K_2Bi_{1-x}Zr(PO_4)_3$:xSm^{3+} (x=0, 0.02, 0.04, 0.06, 0.08, 0.10, 0.12, 0.14) samples and the simulated pattern are shown in Fig. 1. It is obvious that the experimental patterns fit well with the standard one [15] and do not exhibit peaks related to impurities, suggesting that the prepared

$K_2Bi_{1-x}Zr(PO_4)_3$:xSm^{3+} samples have the same crystal structure as the space group $P2_13$. This finding indicates that a single-phase phosphor is obtained and a small doping concentration of Sm^{3+} ions does not measurably influence the crystal structure of the $K_2BiZr(PO_4)_3$ host matrix. According to Shannon's reference, the ionic radius of the Sm^{3+} ion (0.095 8 nm) is similar to that of the Bi^{3+} ion (0.103 nm) of the host lattice in six coordinates with nearby oxygen atoms. Given the effective ionic radii and charge balance, we believe that the 4a site of Bi^{3+} ions were randomly occupied by Sm^{3+} activators. Moreover, the sharp diffraction peaks suggest good crystallinity of the prepared samples.

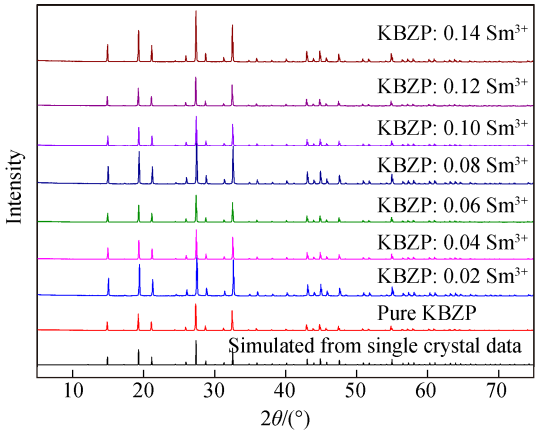


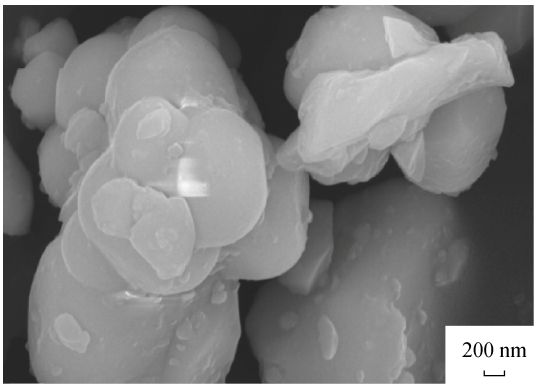
Fig. 1 Simulated X-ray powder diffraction pattern of $K_2BiZr(PO_4)_3$ (KBZP) and X-ray powder diffraction patterns of $K_2Bi_{1-x}Zr(PO_4)_3$:xSm^{3+} (x = 0, 0.02, 0.04, 0.06, 0.08, 0.10, 0.12, 0.14) in the 2θ range of 5°–75°

3.2 Morphology

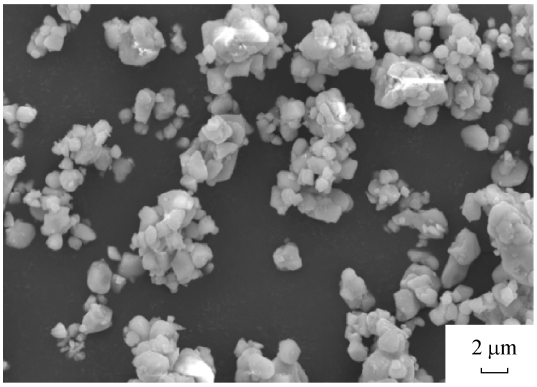
Scanning electron microscopy (SEM) images of polycrystalline $K_2Bi_{0.9}Zr(PO_4)_3$:$0.1Sm^{3+}$ are shown in Fig. 2. It can be clearly seen that the prepared sample is crystalline with irregularly shaped agglomerated particles, a block morphology and a narrow size distribution, which are the inherent characteristics of polycrystalline samples from the traditional solid-state reaction method. The particle sizes are on the micron scale and are distributed between 1 and 5 μm. It is worth noting that some fragments and irregular broken lines are observed due to grinding after calcination in the agate mortar.

3.3 IR and UV-Vis spectra

Fig. 3 shows the IR spectra of orthophosphate $K_2BiZr(PO_4)_3$ in the range of 350–2 000 cm^{-1}, in which the bands can be assigned according to other similar inorganic phosphate compounds [20]. A broad band in the range of 700–1 300 cm^{-1} can be assigned to the asymmetric stretching vibrations (v_3 and v_1) of P–O bonds in the PO_4 tetrahedra. The high frequency band at 1 610 cm^{-1} may be explained by the interaction between P–O and adjacent bonds, Bi–O or Zr–O. The absorption bands at 505–650 cm^{-1} and 420–450 cm^{-1} correspond to the v_4 symmetrical bending vibrations in the PO_4 tetrahedra.



(a) High magnification



(b) Low magnification

Fig. 2 SEM images of $K_2Bi_{0.9}Zr(PO_4)_3$: $0.1Sm^{3+}$

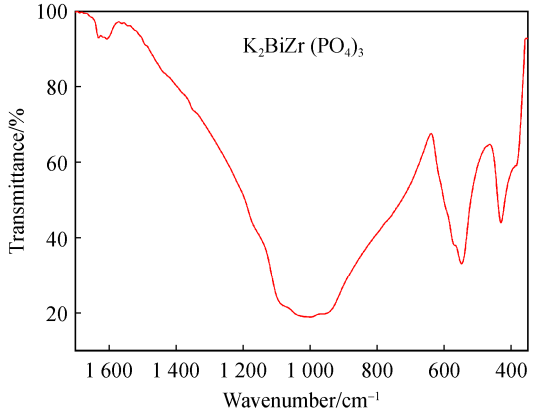


Fig. 3 IR spectrum of $K_2BiZr(PO_4)_3$ in the range of 350–1 700 cm^{-1}

Fig. 4 presents the UV–Vis diffuse reflectance spectrum of polycrystalline $K_2BiZr(PO_4)_3$ in the range of 200–800 nm. The Kubelka-Munk (K-M) function, $\alpha/S = K/S = F(R) = (1-R)^2/2R$ [21], was used to convert the spectrum for estimating the optical absorption cutoff edge, where α is the absorption coefficient, S is the scattering coefficient, K is the absorption and R is the reflectance. The undoped $K_2BiZr(PO_4)_3$ sample does not absorb light energy in the visible range of 400–800 nm,

and strong absorption occurs in the UV light region. This finding suggests that $K_2BiZr(PO_4)_3$ may be used as a good luminescent host matrix because it has less effect on the electronic transitions of the rare earth activators. Moreover, to obtain a more accurate value of the band gap of $K_2BiZr(PO_4)_3$, we plot the (*K*/*S*)-*versus*-*E* scheme (see inset of Fig. 4). The intersection point of the tangent and horizontal axes suggests a band gap of 4.26 eV.

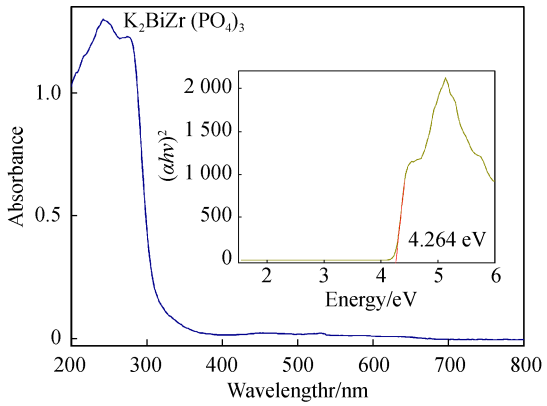


Fig. 4　Experimental UV-Vis absorption spectrum of $K_2BiZr(PO_4)_3$

3.4　Theoretical studies

Fig. 5 presents the band structure of $K_2BiZr(PO_4)_3$ along the high-symmetry points of the first Brillouin zone that is calculated from single crystal data. It can be seen that both the top of the valence bands (VBs) and the bottom of conduction bands (CBs) have little dispersion. It should be noted that the original calculated band gap is 2.23 eV, which is lower than the experimental band gap of 4.26 eV, as mentioned above. This discrepancy may be attributed to the limitation of the density functional theory (DFT) method, which usually underestimates the band gap for an insulator; thus, we use a scissor operator of 2.03 eV to analyze the bond structure and density of states (DOS) of compound $K_2BiZr(PO_4)_3$. Table 1 records the state energies of the lowest conduction band (L-CB) and the highest valence band (H-VB) at the points of Brillouin zone path *X*→*R*→*M*→*G*→*G*→*R*. Both the lowest energy (4.26 eV) of the CBs and the highest energy (0 eV) of the VBs were localized at the *X* point, suggesting that $K_2BiZr(PO_4)_3$ is an insulator with a direct band-gap of 4.26 eV.

To learn more about the nature of the bond structure and to assign the optical absorption of $K_2BiZr(PO_4)_3$, the total and partial DOSs for individual elements were calculated ranging from –49.0 to 12.0 eV. As shown in Fig. 6, the regions below the Fermi level contain 260 bands that can be divided into seven regions. The Zr 4*s* states construct the bottom-most VB region below –45.0 eV, the K 3*s* states form the second region at –28.7 eV, and the Zr 4*p* states constitute the third region at –27.8 eV. The fourth region in the range from –22.5 to –17.8 eV is mainly composed of the mixed states of Bi 5*d*, P 3*s*3*p* and O 2*s*. The strong hybridization between these states expresses the formation of the Bi–O and P–O bonds. The fifth region contains a single peak centered at –12.7 eV due to the K 3*p* states. The sixth region from –9.5 to –0.9 eV is mainly attributed to the mixed states of the P 3*s*3*p* and O 2*p*, which confirms the covalent interaction of P and O. Importantly, the highest VB region from –0.9 to 0.0 eV that is just below the Fermi level is dominated by the O 2*p* states, mixing with a small amount of Bi 6*s* states. On the other hand, the CBs just above the Fermi level (at 4.26 eV) are mainly constructed by the Zr 4*p* states. Therefore, we confirmed that the optical absorption at 4.26 eV results from the O→Zr charge transfer.

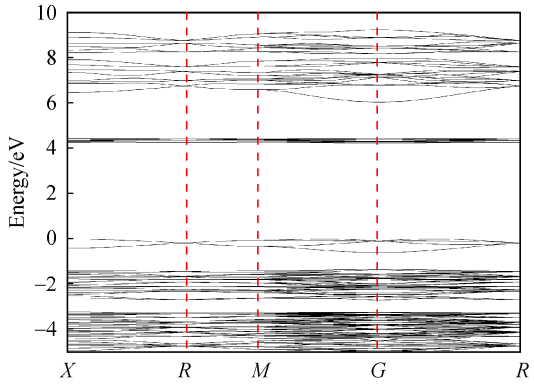


Fig. 5　Band structure of $K_2BiZr(PO_4)_3$ along the high-symmetry points of the first Brillouin zone

Table 1　State energies of the lowest conduction band (L–CB) and the highest valence band (H–VB) at some *k*-points of $K_2BiZr(PO_4)_3$

eV

k-point	*X*(1/2,0,0)	*R*(1/2,1/2,1/2)	*M*(1/2,1/2,0)	*G*(0,0,0)	*R*(1/2,1/2,1/2)
L–CB	4.264	4.265	4.250	4.238	4.265
H–VB	0	–0.172	–0.065	–0.090	–0.172

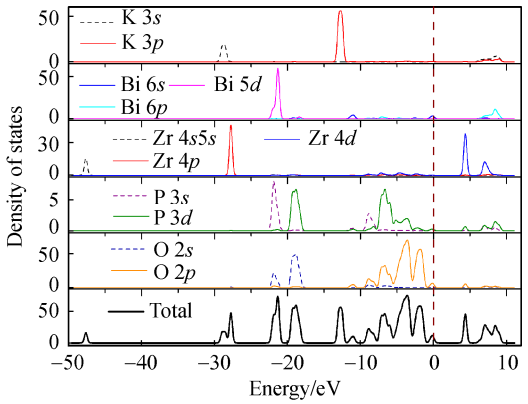


Fig. 6　Total and partial DOSs of $K_2BiZr(PO_4)_3$

3.5　PL properties

The fact that the position of the $K_2BiZr(PO_4)_3$ host sensitization band is independent of the involved rare

earth ions suggests that it can be used as a good luminescent host matrix for various rare earth ion doping. As shown in Fig. 7, the excitation spectrum of $K_2Bi_{0.9}Zr(PO_4)_3$:0.1Sm^{3+} by monitoring 600 nm emission contains a series of sharp bands at approximately 345, 362, 375, 391, 402, 416, 440 and 468 nm, which correspond to the intrinsic 4*f*→4*f* transitions of Sm^{3+}: $^6H_{5/2}$→$^3H_{7/2}$, $^6H_{5/2}$→$^4D_{5/2}$, $^6H_{5/2}$→$^6P_{7/2}$, $^6H_{5/2}$→$^4K_{11/2}$, $^6H_{5/2}$→$^6P_{3/2}$, $^6H_{5/2}$→$^6P_{5/2}$, $^6H_{5/2}$→$^4I_{15/2}$ and $^6H_{5/2}$→$^4I_{13/2,11/2,9/2}$, respectively. It is clear that the O^{2-}→Sm^{3+} charge transfer (CT) band is much weaker than that of *f*→*f* transitions and is even invisible, which matches well with other Sm^{3+}-activated phosphors [22–26]. The series of prepared phosphors $K_2Bi_{1-x}Zr(PO_4)_3$:xSm^{3+} (x = 0.02, 0.04, 0.06, 0.08, 0.10, 0.12, 0.14) do not show different features compared with that for x = 0.10, except for the PL intensity. Therefore, the strong excitation peaks in the near UV range (340–425 nm) ensures that $K_2Bi_{1-x}Zr(PO_4)_3$:xSm^{3+} phosphors can be effectively excited by near-UV LED chips.

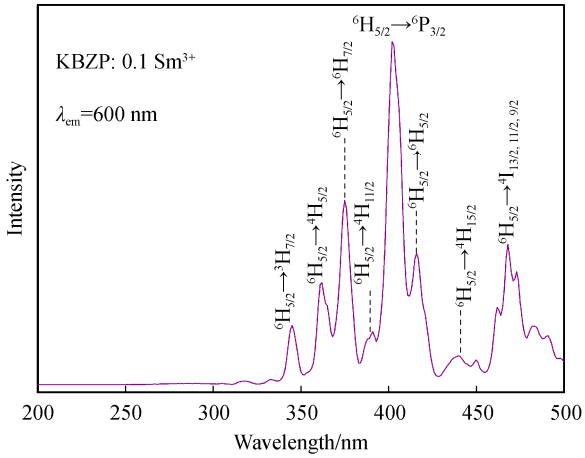
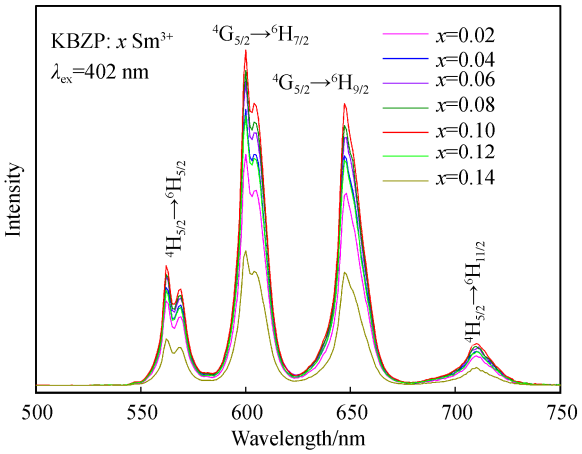
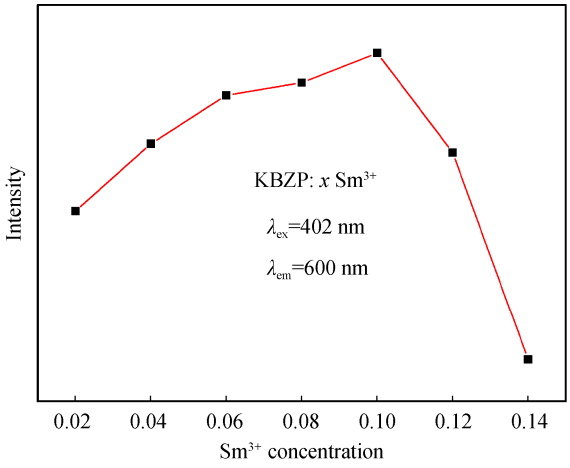


Fig. 7 Excitation spectrum of $K_2Bi_{0.9}Zr(PO_4)_3$:0.1Sm^{3+}

As shown in Fig. 8a, the PL spectrum of $K_2Bi_{0.9}Zr(PO_4)_3$:0.1Sm^{3+} excited by 402 nm light mainly has several distinct groups of peaks in the range of 500–750 nm. There are three strong emissions in the orange-reddish region from positions at 562, 600 and 647 nm, which correspond to the $^4G_{5/2}$→$^6H_{5/2}$, $^4G_{5/2}$→$^6H_{7/2}$ and $^4G_{5/2}$→$^6H_{9/2}$ transitions of Sm^{3+}, respectively [27–28]. In addition, there exists a weak emission centered at 710 nm, which can be assigned to the $^4G_{5/2}$→$^6H_{11/2}$ transitions of Sm^{3+}. It is well known that the emission spectrum of Sm^{3+}-activated phosphor strongly depends on the symmetry of the Sm^{3+} site in the host lattice [29–31]. The $^4G_{5/2}$→$^6H_{5/2}$ transition is the magnetic dipole transition, which scarcely changes the crystal field strength around the Sm^{3+} ions, which is independent of the symmetry, whereas the transition of $^4G_{5/2}$→$^6H_{9/2}$ is the electric dipole transition whose intensity is very sensitive to the site symmetry of the Sm^{3+} activators in the host matrix. Although the $^4G_{5/2}$→$^6H_{7/2}$ emission corresponds to the magnetic dipole transition, its magnetic dipole character is usually very low and dominated by the electric dipole (ED) transition. Hence, if the Sm^{3+} occupies the site in a low symmetry, then the $^4G_{5/2}$→$^6H_{9/2}$ or $^4G_{5/2}$→$^6H_{7/2}$ emission is frequently the strongest, but in a site with an inversion center, the $^4G_{5/2}$→$^6H_{5/2}$ transition becomes dominant. For $K_2Bi_{0.9}Zr(PO_4)_3$:0.1Sm^{3+}, it is obvious that the intensities of $^4G_{5/2}$→$^6H_{9/2}$ and $^4G_{5/2}$→$^6H_{7/2}$ emissions are stronger than those of the $^4G_{5/2}$→$^6H_{5/2}$ emissions, which is in good agreement with the fact that the Sm^{3+} activators substitute the Bi^{3+} sites without an inversion center.



(a) Emission spectra of $K_2Bi_{1-x}Zr(PO_4)_3$:xSm^{3+} (x = 0.02, 0.04, 0.06, 0.08, 0.10, 0.12, 0.14) samples excited by 402 nm as a function of Sm^{3+} doping content x



(b) Variation in 600 nm emission intensity

Fig. 8 Relation of emission intensity with the Sm^{3+} content

These three colors are usually referred to as the 1 931 color coordinates, the current standard for lighting specifications on the market. In general, the color of any light source in this color space can be represented as an (x, y) coordinate. The location of the color coordinates of phosphor $K_2Bi_{0.9}Zr(PO_4)_3$:0.1Sm^{3+} on the CIE chromaticity diagram is presented in Fig. 9. Under excitation at 402 nm, the calculated CIE chromaticity

coordinate is (0.6012, 0.397 3), falling in the orange-reddish region. We may expect that compound $K_2Bi_{0.9}Zr(PO_4)_3$:$0.1Sm^{3+}$ can be used as a good orange-reddish phosphor.

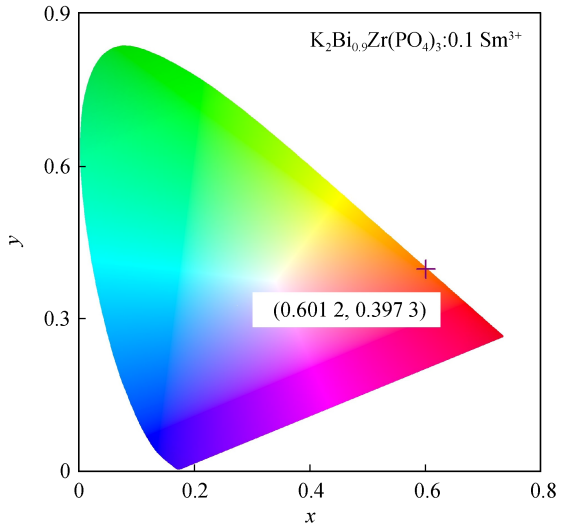


Fig. 9　CIE chromaticity diagram for $K_2Bi_{0.9}Zr(PO_4)_3$:$0.1Sm^{3+}$ with excitation at 402 nm

To study the effect of the Sm^{3+} ion concentration on the emission intensity of the $K_2Bi_{1-x}Zr(PO_4)_3$:xSm^{3+} phosphor, a series of samples with different Sm^{3+} ion concentrations (2%–14%, in mole) were prepared. As shown in Fig. 8, the peak position and shape of the $K_2Bi_{1-x}Zr(PO_4)_3$:xSm^{3+} emission spectra do not vary with Sm^{3+} content. However, the intensity changes along with doping amounts. With increasing Sm^{3+} ion concentration, the emission intensity first increases, reaching a maximum at 10%, and then decreases. The decrease in the emission intensity at high Sm^{3+} ion concentrations can be attributed to concentration quenching. The critical transfer distance (R_c) between two activator ions can be calculated by following equation [32–33]:

$$R_c \approx 2\left(\frac{3V}{4\pi x_c N}\right)^{1/3} \quad (1)$$

where V is the volume of the unit cell, x_c is the atom fraction of Sm^{3+} activator in which the concentration quenching occurs, and N stands for the number of host ions in one-unit cell. For $K_2Bi_{1-x}Zr(PO_4)_3$:xSm^{3+}, the appropriate values of x_c, N and V are 0.10, 2 and 1.087 7 nm^3, respectively. Thus, the R_c value is calculated to be 2.182 nm for responding to the distance of exchange interaction[34].

4　Conclusions

In summary, orange-reddish light emitting $K_2Bi_{1-x}Zr(PO_4)_3$:xSm^{3+} phosphors were synthesized successfully by the traditional solid-state reaction method. The XRD results reveal that at 900 ℃, the synthesized phosphor shows a more crystalline, single phase $K_2BiZr(PO_4)_3$ host. DFT analysis reveals that $K_2BiZr(PO_4)_3$ is an insulator with an indirect band-gap of 4.26 eV, which is suitable for a luminescent host matrix. The average crystallite sizes were found to be in the range of 1–5 μm. The excitation spectra cover a wide range of wavelengths (340–425 nm), which match well with the emissions of near-UV LEDs and bluish green LED chips. The emission spectra showed a characteristic orange-reddish emission at 562, 600 and 647 nm due to the transitions from the excited $^4G_{5/2}$ to ^6H_J (J = 5/2, 7/2, 9/2) levels of the Sm^{3+} activators, respectively. The optimum molar concentration and maximum critical distance between the Sm^{3+} ions were found to be 10 % and 2.182 nm, suggesting an exchange interaction for the concentration quenching mechanism. The CIE coordinates (0.6012, 0.397 3) were close to the white regions of the spectrum. One may expect that Sm^{3+}-doped $K_2BiZr(PO_4)_3$ can be used as orange-reddish phosphor for illumination or displays. Further work on the other Ln^{3+}-activated $K_2BiZr(PO_4)_3$ materials is in progress.

References:

[1] XU Z H, XIA Z G, LIU Q L. Two-step synthesis and surface modification of CaZnOS: Mn^{2+} phosphors and the fabrication of a luminescent poly (dimethylsiloxane) film[J]. Inorg Chem, 2018, 57: 1670−1675.

[2] LI K, VAN DEUN R. Photoluminescence and energy transfer properties of a novel molybdate $KBaY(MoO_4)_3$:Ln^{3+} (Ln^{3+} = Tb^{3+}, Eu^{3+}, Sm^{3+}, Tb^{3+}/Eu^{3+}, Tb^{3+}/Sm^{3+}) as a multi-color emitting phosphor for UV w-LEDs[J]. Dalton Trans, 2018, 47: 6995−7004.

[3] WU D, YE X Y, LIU S B, et al. Structure and luminescence properties of Li^+-doped (Sc Lu)VO_4:Eu^{3+} red phosphors[J]. J Chin Ceram Soc, 2018, 46: 128−135.

[4] SUN J, XU S C, SONG W R, et al. Luminescence property and mechanism of yellow-green long persistent phosphor $Ba_2B_2O_5$:Ce^{3+}, Dy^{3+}[J]. J Chin Ceram Soc, 2017, 45: 1454−1458.

[5] ZHOU J, XIA Z G. Synthesis, luminescence properties and energy transfer behavior of $Na_2CaMg(PO_4)_2$: Eu^{2+}, Mn^{2+} phosphors[J]. J Lumines, 2014, 146: 22−26.

[6] ZHAO D, MA F X, MA S Q, et al. Four-dimensional incommensurate modulation and luminescent properties of host material $Na_3La(PO_4)_2$[J]. Inorg Chem, 2017, 56: 1835−1845.

[7] ATUCHIN V V, SUBANAKOV A K, ALEKSANDROVSKY A S, et al. Structural and spectroscopic properties of new noncentrosymmetric self-activated borate $Rb_3EuB_6O_{12}$ with B_5O_{10} units[J]. Mater Des, 2018, 140: 488−494.

[8] ZHANG X, WU H, WANG Y, et al. Application of the dimensional reduction formalism to $Pb_{12}Li_2(P_2O_7)_2(P_4O_{13})_2(P_4O_{13})$: A phosphate containing three types of isolated P−O Groups[J]. Inorg Chem, 2016, 55: 7329−7331.

[9] SHI Y, WANG Y, PAN S, et al. Synthesis, crystal structures and optical properties of two congruent-melting isotypic diphosphates: $LiM_3P_2O_7$ (M=Na, K)[J]. J Solid State Chem, 2013, 197: 128−133.

[10] HE Z, ZHANG W, CHENG W, et al. Long-range and short-range orderings in $K_4Fe_4P_5O_{20}$ with a natrolite-like framework[J]. Dalton Trans, 2013, 42: 5860−5865.

[11] ZHANG W L, ZHANG H, XIE Z, et al. Syntheses, crystal and electronic structures of two new lead indium phosphates: $Pb_2In_4P_6O_{23}$ and $Pb_2InP_3O_{11}$[J]. Solid State Sci, 2009, 11: 2008−2015.

[12] OGORODNYK I V, ZATOVSKY I V, SLOBODYANIK N S, et al. Synthesis, structure and magnetic properties of new phosphates $K_2Mn_{0.5}Ti_{1.5}(PO_4)_3$ and $K_2Co_{0.5}Ti_{1.5}(PO_4)_3$ with the langbeinite structure[J]. J Solid State Chem, 2006, 179: 3461−3466.

[13] ORLOVA A I, TRUBACH I G, KURAZHKOVSKAYA V S, et al. Synthesis, characterization, and structural study of $K_2FeZrP_3O_{12}$ with the langbeinite structure[J]. J Solid State Chem, 2003, 173: 314−318.

[14] TRUBACH I G, BESKROVNYI A I, ORLOVA A I, et al. Synthesis and investigation of the new phosphates $K_2LnZr(PO_4)_3$ (Ln = Ce-Yb, Y) with langbeinite structure[J]. Crystallogr Rep, 2004, 49: 614−618.

[15] CHORNII V, HIZHNYI YU, NEDILKO S G, et al. Synthesis, srystal structure, luminescence and electronic band structure of $K_2BiZr(PO_4)_3$ phosphate compound[J]. Solid State Phenom, 2015, 230: 55−61.

[16] SEGALL M D, LINDAN P J D, PROBERT M J, et al. First-principles simulation: Ideas, illustrations, and the CASTEP code[J]. J Phys Condens Matter, 2002, 14: 2717−2744.

[17] PERDEW J P, BURKE K, ERNZERHOF M. Generalized gradient approximation made simple[J]. Phys Rev Lett, 1996, 77: 3865−3868.

[18] PAYNE M C, TETER M P, ALLAN D C, et al. Iterative minimization techniques for ab initio total-energy calculations: Molecular dynamics and conjugate gradients[J]. Rev Mod Phys, 1992, 64: 1045−1-53.

[19] PACK J D, MONKHORST H J. Special points for Brillonln-zone integrations—A reply[J]. Phys Rev B, 1977, 16: 1748−1749.

[20] BADRI A, JABLI M, WATTIAUX A, et al. Crystal structure, Mössbauer spectroscopy and dye adsorption properties of a new layered iron phosphate $RbMgFe(PO_4)_2$[J]. J Mole Struct, 2018, 1167: 161−168.

[21] WENDLANDT W M, HECHT H G. Reflectance spectroscopy[M]. Interscience: New York, 1966: 156−160.

[22] ZHAO D, MA F X, LIU B Z, et al. Syntheses, crystal structure and luminescent properties of polyborates $PbLnB_7O_{13}$ (Ln = Gd, Sm) with a 2D B_7O_{13} (infinity) framework[J]. J Lumin, 2018, 195: 134−140.

[23] GUPTA P, BEDYAL A K, KUMAR V, et al. Energy transfer mechanism from Gd^{3+} to Sm^{3+} in $K_3Gd(PO_4)_2$:Sm^{3+} phosphor[J]. Mater Res Exp, 2015, 2: 076202.

[24] RYBA-ROMANOWSKI W, LISIECKI R, BEREGI E, et al. Spontaneous and stimulated emission in Sm^{3+}-doped $YAl_3(BO_3)_4$ single crystal[J].J Lumin, 2015, 167: 163−166.

[25] LIU H Y, LI M F, WANG Z P, et al. Enhanced luminescence intensity of $Ca_9Al(PO_4)_7$: Sm^{3+} by introducing Ce^{3+} as sensitizer[J]. J Chin Ceram Soc, 2018, 46: 1453–1457.

[26] ZHAO D, NIE C K. Synthesis and multi–color luminescent properties of Tb^{3+}/Sm^{3+}-codoped $K_3Gd_3B_4O_{12}$ phosphor[J]. J Liaocheng Univ, 2019, 32: 85−89.

[27] KACZKAN M, BORUC Z, TURCZYNSKI S, et al. Site-selective laser spectroscopy of Sm^{3+} ions in $Y_4Al_2O_9$[J]. J Lumin, 2016, 170: 330−335.

[28] ZHOU R, WANG L, XU M, et al. Photoluminescence characteristics of Sm^{3+} doped $Sr_2P_2O_7$ as new orange-red emitting phosphor[J]. J Alloys And Compd, 2015, 647: 136−140.

[29] HAN B, ZHANG L, LI P, et al. Photoluminescence properties of novel yellowish orange emitting phosphor $KBaBP_2O_8$: Sm^{3+}[J]. Mater Lett, 2014, 126: 113−115.

[30] ZHAO D, NIE C K, TIAN Y, et al. A new luminescent host material $K_3GdB_6O_{12}$: Synthesis, crystal structure and luminescent properties activated by Sm^{3+}[J]. Z Kristallogr Cryst Mater, 2018, 233: 411−419.

[31] ZHAO D, NIE C K, Synthesis and multi-color luminescent properties of Tb^{3+}/Sm^{3+}-codoped $K_3Gd_3B_4O_{12}$ phosphor[J]. J Liaocheng Univ (Nat Sci), 2019, 32: 85−89.

[32] CHEN P, HU W, YANG D, et al. Ba_2ZnWO_6: Sm^{3+} as promising orange-red emitting phosphors: Photoluminescence properties and energy transfer process[J]. Phys B, 2018, 530: 127−132.

[33] LIU Q, WANG L, HUANG W, et al. Red-emitting double perovskite phosphors $Sr_{1-x}Ca_xLaMgSbO_6$: Eu^{3+}: Luminescence improvement based on composition modulation[J]. Ceram Int, 2017, 43: 16292−16299.

[34] LAI Y, LI K, QIAO G, et al. Structure and magnetic properties of layered compounds $RMn_{1.7}Cr_{0.3}Si_2C$ (R = Nd, Sm, Dy)[J]. J Alloy Compd, 2018, 746: 238−243.